

# Testing General Relativity with X-ray reflection spectroscopy: The Konoplya-Rezzolla-Zhidenko parametrization

Sourabh Nampalliwar,<sup>1,\*</sup> Shuo Xin,<sup>2</sup> Shubham Srivastava,<sup>3</sup> Askar B. Abdikamalov,<sup>4</sup> Dimitry Ayzenberg,<sup>4</sup> Cosimo Bambi,<sup>4</sup> Thomas Dauser,<sup>5</sup> Javier A. García,<sup>6,5</sup> and Ashutosh Tripathi<sup>4</sup>

<sup>1</sup>*Theoretical Astrophysics, Eberhard-Karls Universität Tübingen, 72076 Tübingen, Germany*

<sup>2</sup>*School of Physics Sciences and Engineering, Tongji University, Shanghai 200092, China*

<sup>3</sup>*Indian Institute of Technology, Kharagpur 721302, India*

<sup>4</sup>*Center for Field Theory and Particle Physics and Department of Physics, Fudan University, 200438 Shanghai, China*

<sup>5</sup>*Remeis Observatory & ECAP, Universität Erlangen-Nürnberg, 96049 Bamberg, Germany*

<sup>6</sup>*Cahill Center for Astronomy and Astrophysics, California Institute of Technology, Pasadena, CA 91125, USA*

X-ray reflection spectroscopy is a promising technique for testing general relativity in the strong field regime, as it can be used to test the Kerr black hole hypothesis. In this context, the parametrically deformed black hole metrics proposed by Konoplya, Rezzolla & Zhidenko (Phys. Rev. D93, 064015, 2016) form an important class of non-Kerr black holes. We implement this class of black hole metrics in RELXILL\_NK, which is a framework we have developed for testing for non-Kerr black holes using X-ray reflection spectroscopy. We compare the results from this new model in the Kerr limit with existing codes, illustrate the effect of the leading deformation parameters on the X-ray reflection spectrum and present constraints on some KRZ parameters using data from the supermassive black hole in Ark 564.

## I. INTRODUCTION

Einstein's theory of gravity, since its proposition over a century ago, has been applied to a variety of astrophysical phenomena in our Universe. Over these years, it has emerged as the standard framework for describing the spacetime in the presence of gravitational objects. While largely successful in the weak-field tests [1], only recently the strong-field predictions of Einstein's gravity (the general theory of relativity, GR hereafter) have become testable in a variety of ways. [2, 3] Presence of a zoo of *alternative theories of gravity*, which address shortcomings of GR with respect to observations e.g., dark matter and dark energy, and/or extend GR to overcome issues e.g., difficulties in quantizing GR and resolution of the curvature singularity, make it crucial to test the strong-field predictions of GR with the latest techniques and technologies.

Black holes are surprisingly ubiquitous objects in our Universe, and due to strong gravity regions in their neighborhoods, form the perfect candidates for testing theories of gravity. Within GR, under reasonable assumptions, a BH is an extremely simple object and its effect on the spacetime is described by very few parameters. Most commonly, these are the BH *mass* and *spin*, making it a Kerr BH. [4] The assumption that astrophysical BHs are described by the Kerr solution is known as the *Kerr hypothesis*. (For the specific conditions and assumptions, see [5].) Alternative theories of gravity often introduce additional parameters, deforming the BH away from the Kerr solution. Observations of effects of BH have been a celebrated exercise in physics, given the potential for discovery of interesting phenomena. Some of the ways these

observations are done are: X-ray spectroscopy (first measurements of BH spin), gravitational wave interferometry (first observation of coalescence of a pair of BHs), pulsar timing (first indirect detection of gravitational waves) and black hole imaging (expected to provide first images of the black hole shadow).

In this work, our focus is on the technique of X-ray spectroscopy. In particular, we are interested in the reflection spectrum of BHs with accretion disks, which is in the X-ray band. Since the gravity of the BH affects its neighborhood and photons that travel from the neighborhood to us, the analysis of the reflection spectrum can be used to study the nature of BH itself. [2, 6] The most advanced model for calculation of the reflection spectrum in the Kerr case is RELXILL. [7, 8] Some of us have extended this model to RELXILL\_NK, which can calculate the reflection spectrum for non-Kerr metrics. [9] (Recently, a public version of RELXILL\_NK has appeared, See [10].) The model has been applied to X-ray observations of several astrophysical BHs to place constraints on deviations away from the Kerr solution. [11–21]

The non-Kerr metric most commonly used with RELXILL\_NK is the one proposed by Johannsen [22] (See also [23]). This metric, referred to as the Johannsen metric hereafter, albeit not a solution of a well-defined alternative theory of gravity, attempts to map BH solutions from several alternative theories. In this sense, it is a good candidate for theory-agnostic tests of the Kerr hypothesis. In this paper, we present the application of another such metric to RELXILL\_NK. This metric has been proposed by Konoplya, Rezzolla and Zhidenko [24], and we will refer to it as the KRZ metric hereafter.

The paper is organized as follows: in Sec. II, we review the RELXILL\_NK framework, the KRZ metric and the numerical methods involved. Sec. III compares various quantities in the new model with the existing codes, and Sec. IV illustrates how these quantities are affected

\* Corresponding author: [sourabh.nampalliwar@uni-tuebingen.de](mailto:sourabh.nampalliwar@uni-tuebingen.de)

by the KRZ parameters. In Sec. V, the new model is applied to X-ray observations of a supermassive BH. Conclusions follow in Sec. VI.

## II. REVIEW

### A. The KRZ metric

Non-Kerr metrics can be classified in two categories. The *top-down* metrics are those which are obtained as a solution of an alternative theory of gravity, e.g., the Einstein-dilaton-Gauss-Bonnet BHs [25–30], the Chern-Simons BHs [31–34], and the Kerr-Sen BHs [35–38]. The *bottom-up* metrics on the other hand are obtained not from alternative theories of gravity but by generalizing the Kerr metric. Each class has its advantages and disadvantages. Top-down metrics are difficult to obtain and may only be available in a numerical form, but testing for them amounts to testing an alternative theory of gravity.

Bottom-up metrics may have pathologies in the space-time for parameter ranges, but they can be mapped to several top-down metrics and thus constraints on parameters of bottom-up metrics translates to constraints on several top-down metrics. The Johannsen metric implemented in RELXILL\_NK is one example of a bottom-up metric. Here we review another bottom-up metric that we have implemented in RELXILL\_NK, the KRZ metric.

The KRZ metric is based on a generic stationary and axisymmetric metric in the usual  $(t, r, \theta, \phi)$  coordinates. The metric functions are written in terms of continued fraction expansions in the polar and radial coordinates. This approach has the benefit of a superior convergence with fewer parameters than expansions in  $M/r$  (as is the case in the Johannsen metric) when mapping to top-down metrics.

Assuming reflection symmetry across the equatorial plane and neglecting coefficients of higher orders, the line element of the KRZ metric reads

$$ds^2 = -\frac{N^2 - W^2 \sin^2 \theta}{K^2} dt^2 - 2Wr \sin^2 \theta dt d\phi + K^2 r^2 \sin^2 \theta d\phi^2 + \frac{\Sigma B^2}{N^2} dr^2 + \Sigma r^2 d\theta^2, \quad (1)$$

where

$$\begin{aligned} N^2 &= \left(1 - \frac{r_0}{r}\right) \left(1 - \frac{\epsilon_0 r_0}{r} + (k_{00} - \epsilon_0) \frac{r_0^2}{r^2} + \frac{\delta_1 r_0^3}{r^3}\right) + \left((k_{21} + a_{20}) \frac{r_0^3}{r^3} + \frac{a_{21} r_0^4}{r^4}\right) \cos^2 \theta, \\ B &= 1 + \frac{\delta_4 r_0^2}{r^2} + \frac{\delta_5 r_0^2}{r^2} \cos^2 \theta, \quad \Sigma = 1 + \frac{a_*^2}{r^2} \cos^2 \theta, \\ W &= \frac{1}{\Sigma} \left(\frac{w_{00} r_0^2}{r^2} + \frac{\delta_2 r_0^3}{r^3} + \frac{\delta_3 r_0^3}{r^3} \cos^2 \theta\right), \\ K^2 &= 1 + \frac{a_* W}{r} + \frac{1}{\Sigma} \left(\frac{k_{00} r_0^2}{r^2} + \left(\frac{k_{20} r_0^2}{r^2} + \frac{k_{21} r_0^3}{r^3 \left(1 + \frac{k_{22}(1 - \frac{r_0}{r})}{1 + k_{23}(1 - \frac{r_0}{r})}\right)}\right) \cos^2 \theta\right). \end{aligned} \quad (2)$$

This form of the metric was first used by some of us in a preliminary investigation of the KRZ metric. [39] The six *deformation parameters*  $\{\delta_j\}$  ( $j = 1, 2, \dots, 6$ ), are related to the coefficients appearing in the KRZ metric (as it was first defined by Konoplya, Rezzolla & Zhidenko in [24]) by the following relations

$$\begin{aligned} r_0 &= 1 + \sqrt{1 - a_*^2}, \quad \epsilon_0 = \frac{2 - r_0}{r_0}, \\ a_{20} &= \frac{2a_*^2}{r_0^3}, \quad a_{21} = -\frac{a_*^4}{r_0^4} + \delta_6, \\ k_{00} &= k_{22} = k_{23} = \frac{a_*^2}{r_0^2}, \quad k_{20} = 0, \\ k_{21} &= \frac{a_*^4}{r_0^4} - \frac{2a_*^2}{r_0^3} - \delta_6, \quad w_{00} = \frac{2a_*}{r_0^2}. \end{aligned}$$

Here the mass is  $M = 1$  and  $a_*$  is the spin parameter.  $r_0$  is the radial coordinate in the equatorial plane of the

event horizon. The physical interpretation of the deformation parameters can be summarized as follows (see Ref. [39] for more details):

$$\begin{aligned} \delta_1 &\rightarrow \text{deformations of } g_{tt}, \\ \delta_2, \delta_3 &\rightarrow \text{rotational deformations of the metric,} \\ \delta_4, \delta_5 &\rightarrow \text{deformations of } g_{rr}, \\ \delta_6 &\rightarrow \text{deformations of the event horizon.} \end{aligned}$$

With this choice, the mass-quadrupole moment is the same as in the Kerr metric, and deviations from the Kerr solution are only possible in the strong gravity region. In this paper, we will focus our attention on  $\delta_1$  and  $\delta_2$ , which are expected to have the strongest impact on the quantities of interest in this work (e.g., the innermost stable circular orbit (ISCO hereafter), redshift, etc.). Note that currently RELXILL\_NK allows for variation in one deformation parameter at a time, so we will analyze the effect

of  $\delta_1(\delta_2)$ , while keeping  $\delta_2(\delta_1)$  and all other deformation parameters zero.

### B. The Xspec model

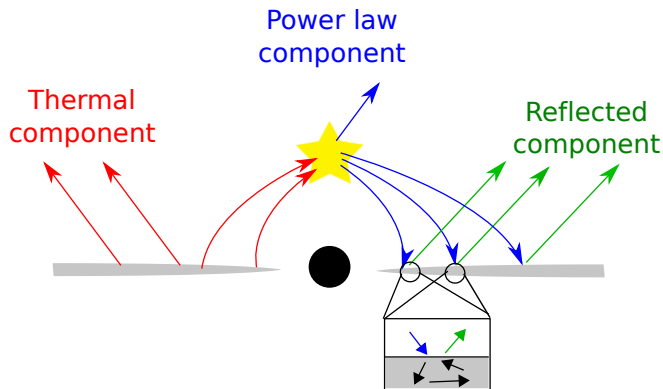


FIG. 1. Schematic of the BH-accretion disk-corona system. The BH is colored black, the disk grey and the corona yellow. Various radiation components are labeled. The inset shows conversion of incident radiation in to reflected radiation.

The standard model for a BH-accretion disk system is the disk-corona model. [40] The BH is assumed to be surrounded by a geometrically thin and optically thick disk [41],<sup>1</sup> with its inner edge at some radius  $r_{\text{in}}$  at the ISCO at its closest, and the outer edge at some large radius  $r_{\text{out}}$ . In addition, the system possesses a “corona”,

$$F_o(\nu_o) = \int I_o(\nu_o, X, Y) d\tilde{\Omega} = \frac{1}{D^2} \int_{r_{\text{in}}}^{r_{\text{out}}} \int_0^1 \pi r_e \frac{g^2}{\sqrt{g^*(1-g^*)}} f(g^*, r_e, i) I_e(\nu_e, r_e, \vartheta_e) dg^* dr_e. \quad (3)$$

Here  $I_o$  and  $I_e$  are the specific intensity of the radiation (for instance, in units  $\text{erg s}^{-1} \text{cm}^{-2} \text{str}^{-1} \text{Hz}^{-1}$ ) detected by the distant observer and the emitter respectively, related via the Liouville’s theorem as follows:  $I_o = g^3 I_e$ ;  $g = \nu_o/\nu_e$  is the redshift factor,  $\nu_o$  is the photon frequency as measured by the distant observer, and  $\nu_e$  is the photon frequency in the rest frame of the emitter.  $r_e$  is the emission radius in the disk and  $\vartheta_e$  is the photon’s direction relative to the disk at the point of emission.  $X$  and  $Y$  are the Cartesian coordinates of the image of the disk in the plane of the distant observer,  $D$  is the distance of the observer from the source, and  $d\tilde{\Omega} = dXdY/D^2$  is the element of the solid angle subtended by the image of

<sup>1</sup> Various other disk structures are possible. Studies of their effect on the reflection spectrum in the presence of non-Kerr metrics is underway.

which is a thought to be a cloud of hotter (relative to the disk) gas. Fig. 1 illustrates the system under discussion. The disk emits as a blackbody locally and as a multi-temperate blackbody when integrated radially (labeled the *thermal component* in Fig. 1). Inverse Compton scattering of the thermal component by the corona produces X-rays (labeled the *power-law component* in Fig. 1), some of which returns to the disk and is reflected (labeled the *reflected component* in Fig. 1).

Modeling the reflection component requires some understanding of the various physical parameters of disk-corona model. RELXILL\_NK has several parameters to account for the different aspects of the system. These include the inner and outer edge of the disk, inclination of the disk relative to the observer, the disk’s elemental constitution and their ionization, and the emissivity profile. The emissivity profile determines the reflection spectrum at the source, i.e., at the disk, and depends strongly on the coronal geometry. Since the latter is poorly understood, unless in specific cases like the lamp-post geometry, the emissivity profile is modeled by a power-law (intensity  $\propto 1/r^q$ ) or a broken power-law (intensity  $\propto 1/r^a$  for  $r \leq r_{\text{br}}$  and  $\propto 1/r^b$  for  $r > r_{\text{br}}$ ). The spacetime parameters are the BH spin and deformation parameters (present in non-Kerr metrics), if any.

### C. Transfer function

One of the most important quantities in our framework is the transfer function first defined by Cunningham. [42] It appears in the calculation of the flux as follows:

the disk in the observer’s sky. The transfer function  $f$  is defined as

$$f(g^*, r_e, i) = \frac{1}{\pi r_e} g \sqrt{g^*(1-g^*)} \left| \frac{\partial(X, Y)}{\partial(g^*, r_e)} \right|. \quad (4)$$

The normalized redshift factor  $g^*$  is defined as

$$g^* = \frac{g - g_{\text{min}}}{g_{\text{max}} - g_{\text{min}}}, \quad (5)$$

where  $g_{\text{max}} = g_{\text{max}}(r_e, i)$  and  $g_{\text{min}} = g_{\text{min}}(r_e, i)$  are, respectively, the maximum and the minimum values of the redshift factor  $g$  at a constant  $r_e$  and for a given viewing angle of the observer. The  $r_e$ -integral ranges from the inner to the outer edge of the disk, whereas the  $g^*$ -integral ranges from 0 to 1.

The transfer function separates the spacetime effects like the motion of gas and photons (encoded in the transfer function) from the local microphysics (encoded in the

specific intensity at the emission point), and thus acts as an integration kernel for the calculation of flux. Such a separation enables quick computation of the reflection spectrum from a grid of transfer functions for any intensity profile, without the need to retrace photon trajectories, making analysis of X-ray reflection data with RELXILL\_NK convenient.

#### D. Numerical method

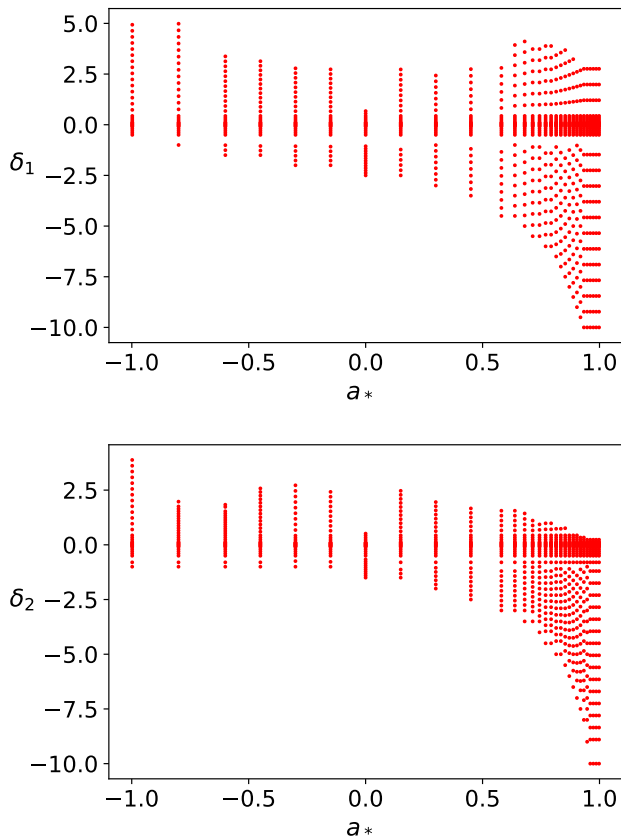


FIG. 2. Points in the spin-deformation parameter grid where transfer functions are calculated, for  $\delta_1$  (top panel) and  $\delta_2$  (bottom panel). See the text for more details.

The numerical method has been presented in great detail earlier. (See [9, 10].) Here we briefly review it.

The most important outcome for each deformation parameter is a FITS table which stores the transfer functions. The table has a grid in three dimensions: spin  $a_*$ , deformation parameter  $\delta$ , and inclination angle  $i$ . The grid points in the  $a_*$  and  $i$  dimension are non-uniform, mutually independent and follow the scheme in RELXILL. The points in the  $\delta$  dimension depend on the spin parameter: the points are chosen such that the ISCO radii at each  $a_*$ , for the range of  $\delta$  at that  $a_*$ , span the range from the minimum Kerr ISCO radius to the maximum Kerr ISCO radius. The resultant grid has a non-uniform

range for  $\delta$  which, although tricky to handle in RELXILL\_NK, is optimal to achieve sufficient resolution for the interpolation later. The spin- $\delta_1$  and spin- $\delta_2$  grids are shown in Fig. 2, in the left and right panels respectively.

At each grid point (namely a specific  $a_*$ ,  $\delta$ , and  $i$  value in the FITS table), the accretion disk is modeled with a grid of 100 emission radii  $r_e$  and 20 equally spaced values of  $g^*$  on each branch.<sup>2</sup> Photons are back-traced from the observer plane to the accretion disk. An adaptive algorithm fine-tunes the coordinates on the observer plane so that the photon when back-traced lands at the exact  $r_{\text{em}}$ . For each such “central” photon, the redshift, emission angle, etc. are calculated and four photons, closely spaced in the observer plane, are launched, to calculate the Jacobian and subsequently the transfer function. An interpolation routine then computes these quantities on the 20 equally spaced values of  $g^*$ , which is stored in the FITS table.

### III. COMPARISON WITH EXISTING CODES

To ensure that the data in the FITS table is accurate, in this section we compare a few quantities calculated in our model with existing codes. Firstly, we compare the transfer functions in our model with those from the standard Kerr case. The plots in Fig. 3 show the transfer functions, at two values of spin ( $a_* = 0.9982$  in the top panels,  $a_* = -0.6$  in the bottom panels), one inclination angle ( $i = 38.87^\circ$ ), three different emission radii, and 40 values of  $g^*$ . The deformation parameters are all set to zero. The values for all these parameters are taken from the grid described in IID, and therefore the transfer function values can simply be read from the FITS table, without requiring further interpolation. The values have excellent agreement, even when the transfer function has relatively large gradients. The only difference is in the points closest to  $g^* = 0$  or 1, and is a consequence of the interpolation method used to construct the FITS table.

We next compare single line shapes (specifically, the iron line with rest-frame emission line energy  $E = 6.4$  keV) from RELLINE\_NK with those from RELLINE.<sup>3</sup> The agreement of the RELLINE model with other existing codes has been shown previously. [43] In Fig. 4, we plot the iron lines for a fixed inclination angle ( $i = 30^\circ$ ) and three different spins,  $-0.8$ ,  $0.5$  and  $0.8$ . The deformation parameters are again set to zero. As the plots suggest, the agreement between two lines is mostly very good, with the relative differences within 1% for most of the energy range, and increasing up to 10% at the low energy end of the spectrum.

<sup>2</sup> Because of the way the transfer function is defined in Eq. 4, it goes to zero when the redshift is maximum or minimum, resulting in two branches of transfer function between  $g^* = 0$  and  $g^* = 1$ .

<sup>3</sup> RELLINE\_NK is the non-Kerr extension of RELLINE. For details, see [10].

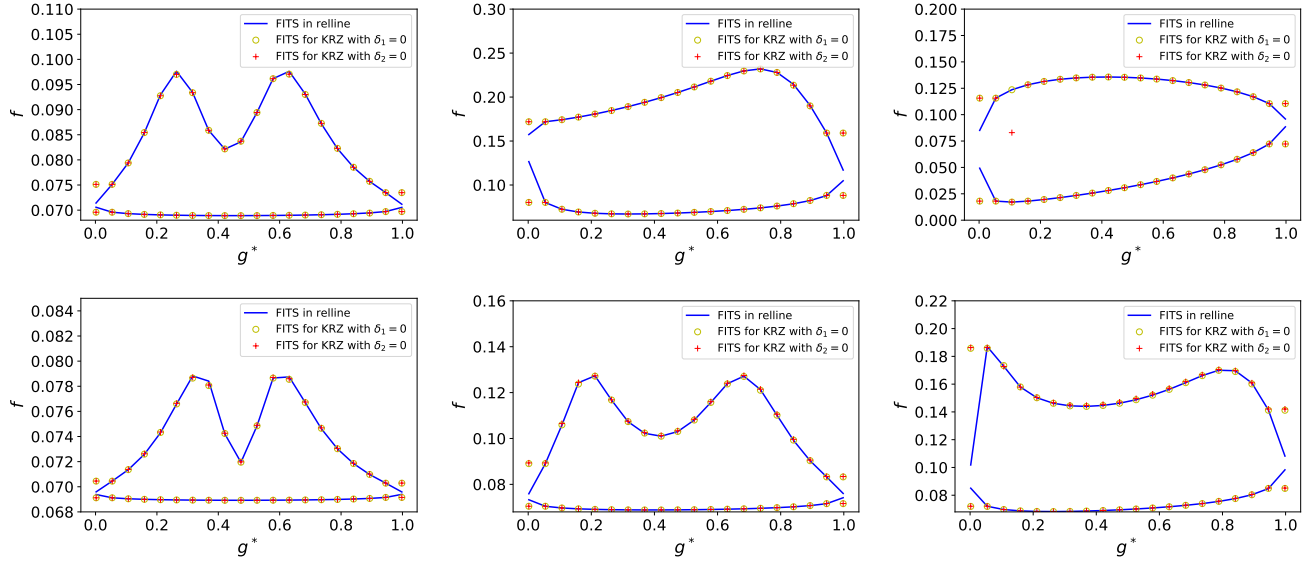


FIG. 3. Comparison between the transfer functions calculated with our code and in the FITS tables of RELXILL. The values of various parameters are:  $a_* = 0.9982$  (top panel),  $a_* = -0.6$  (bottom panel), inclination angle  $i = 38.87^\circ$  in all panels, emission radii (in units of  $M$ ): 69.36 (top left), 4.452 (top middle), 1.228 (top right; at ISCO), 239.3 (bottom left), 25.83 (bottom middle) and 7.856 (bottom right; at ISCO).

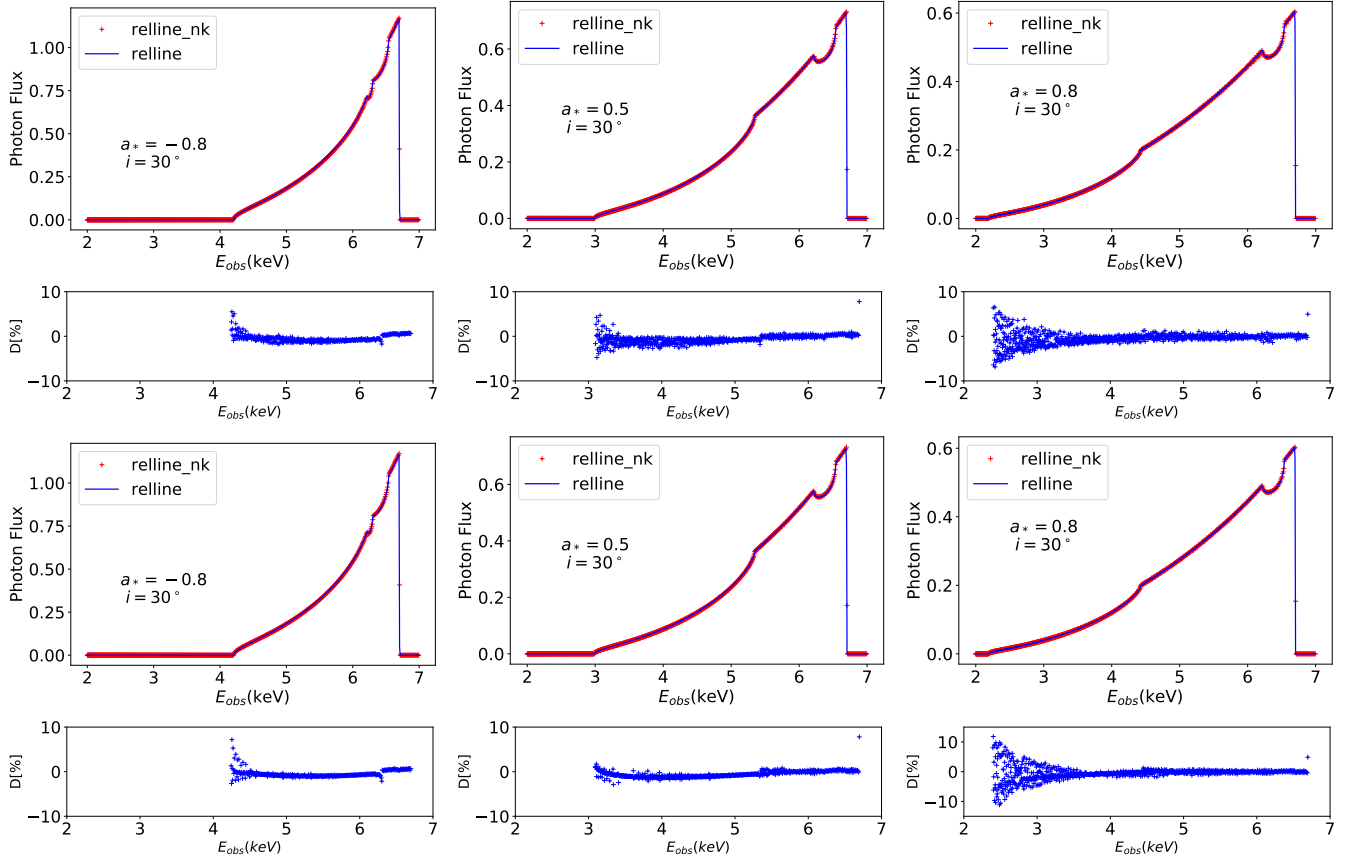


FIG. 4. Comparison between iron lines generated by RELLINE (solid blue line) and by RELLINE\_NK (red crosses) for  $\delta_1$  (top panels) and  $\delta_2$  (bottom panels). The relative differences are shown under each plot. Deformation parameters are set to zero, spin and inclination are indicated in each panel.

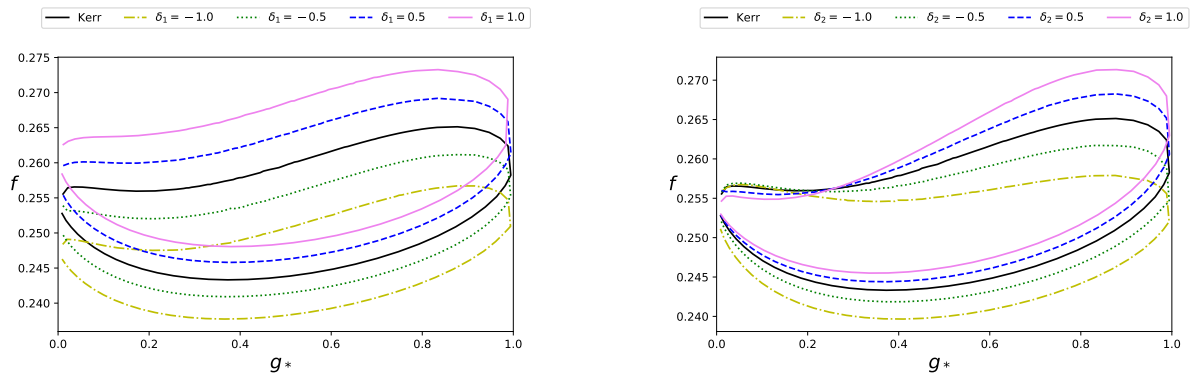


FIG. 5. Impact of  $\delta_1$  (left panel) and  $\delta_2$  (right panel) on the transfer function. The fixed parameters are:  $a_* = 0.8$ ,  $i = 30^\circ$ ,  $r_{\text{em}} = 6M$ .

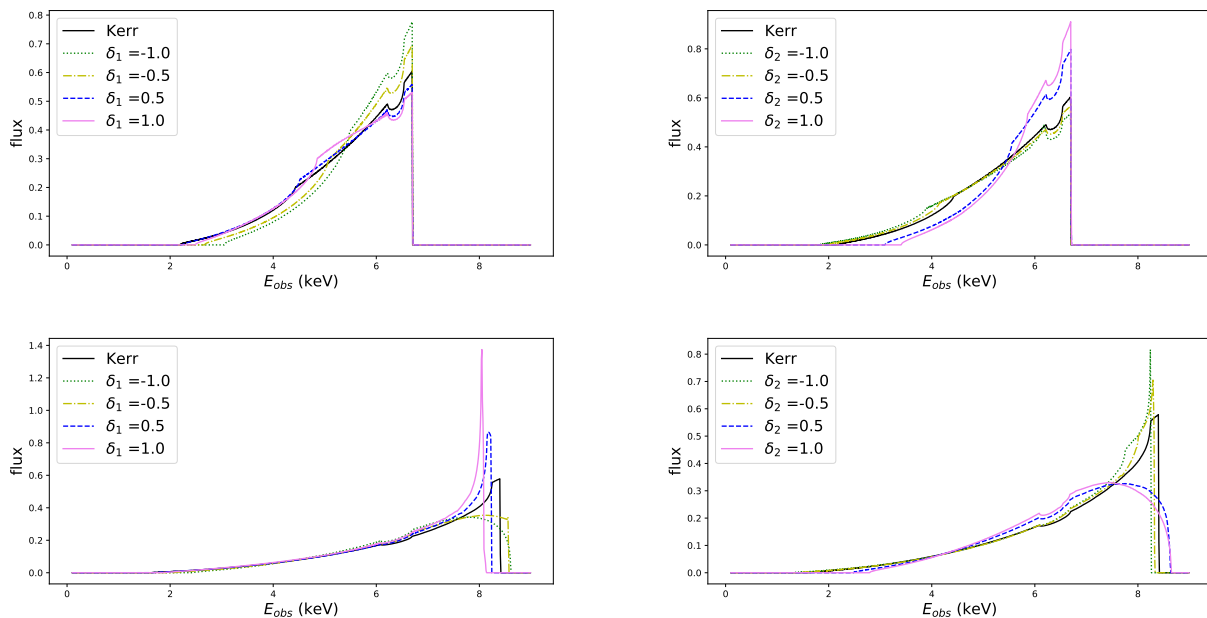


FIG. 6. Impact of  $\delta_1$  (left panels) and  $\delta_2$  (right panels) on the iron line. The fixed parameters are:  $a_* = 0.8$ ,  $i = 30^\circ$  (top panels) and  $70^\circ$  (bottom panels). The rest-frame emission line energy is  $E = 6.4$  keV, inner edge  $r_{\text{in}} = r_{\text{ISCO}}$  and outer edge  $r_{\text{out}} = 400M$ . Local emission spectrum is a power law with emissivity index equal to 3, i.e.,  $I_e \propto 1/r_e^3$ .

#### IV. EFFECTS OF NON-ZERO KRZ PARAMETERS

The additional parameters of the KRZ metric each affect the reflection spectrum in a different way, depending on the modification to the metric they introduce. Since different metric components affect the photon trajectory, redshift, etc. in different ways, those deformation parameters that have a stronger effect on these quantities can in turn be constrained more strongly. To illustrate the effect of the deformation parameters, we first look at the transfer function. Fig. 5 shows how the transfer function (for a fixed  $a_* = 0.8$ ,  $r_{\text{em}} = 6M$ ,  $i = 30^\circ$ ) changes with deformation parameters.

While the change in the transfer function is quite apparent, the transfer function is a mathematical construct and it is difficult to imagine the corresponding change in observable quantities which will eventually be used to constrain the deformation parameters. Therefore, we look at the shape of the iron line, which is much more intuitive. Fig. 6 shows the iron lines for a few configurations, with a fixed spin  $a_* = 0.8$ , two different inclination angles and five different deformation parameters. In the model used to calculate the line shape, we set the emission line energy  $E = 6.4$  keV. The inner edge of the disk is at  $r_{\text{ISCO}}$  and the outer edge is set to be  $400M$ . The emissivity profile is assumed to be a power law with index equal to 3. We observe that the shape of the iron line

too changes. The change is more rapid for positive values than negative values for  $\delta_1$ , and vice versa for  $\delta_2$ . The effect is more pronounced at larger inclination angles.

We can make a qualitative comparison of these KRZ parameters with the Johannsen parameters, in terms of their effect on the iron line. Plots similar to Fig. 6 are presented in Fig. 7 in [9] for the Johannsen parameters. Comparing the two, we observe that both  $\delta_1$  and  $\delta_2$  affect the iron line at a level comparable to  $\alpha_{13}$  and  $\alpha_{22}$ , and at a stronger level than  $\alpha_{52}$  and  $\epsilon_3$ .

## V. SPECTRAL ANALYSIS OF ARK 564 DATA

In this section, we use our newly developed model in the analysis of an X-ray observation. We report our analysis of the *Suzaku* observation of the supermassive black hole in Ark 564 [44].

### A. Review

Ark 564 is classified as a narrow line Seyfert 1 galaxy at redshift  $z = 0.0247$ . Since first observations with *XMM-Newton* in 2000/2001, it has been studied by several authors since it appears as a very bright source in the X-ray band. It is a suitable candidate for tests of general relativity for the following reasons. Firstly, previous studies have shown that the inner edge of the disk may be very close to the central object, which maximizes the signatures of the strong gravity region. [44] Secondly, the source has a simple spectrum. There is no obvious intrinsic absorption to complicate the determination of the reflected emission. The same dataset was analyzed by some of us in [12] to constrain the Johannsen parameters  $\alpha_{13}$  and  $\alpha_{22}$ . Therein, this source and this dataset was found to be easy to analyze and provided good constraints on  $\alpha_{13}$  and  $\alpha_{22}$ .

### B. Observations and data reduction

*Suzaku* observed Ark 564 on 26-28 June 2007 (Obs. ID 702117010) for about 80 ks. For low energies ( $< 10$  keV), *Suzaku* has four co-aligned telescopes which are used to collect photons onto its CCD detectors X-ray Imaging Spectrometer (XIS). XIS is comprised of four detectors; XIS0, XIS2, and XIS3 are front-illuminated and XIS1 is back-illuminated. We only used data from the front-illuminated chips because XIS1 has a lower effective area at 6 keV and a higher background at higher energies. XIS2 data were not used in our analysis because of the anomaly after 9 November 2006.

We have used HEASOFT version 6.24 and CALDB version 20180312 for the data reduction. AEPipeline script of the HEASOFT package has been used for reprocessing and screening of the raw data. The ftool XSELECT and ds9 were used to extract the XIS source and

background spectrum from a 3.5 arc minute radius. The background region was selected as far as possible from the source so as to avoid contamination. The RMF file was generated using XISRMFGEN and the ARF file which corresponds to effective area of the telescope was generated using XISSIMARFGEN. At last, the final source spectrum, background spectrum and response file were generated by combining the data from XIS0 and XIS3 using ADDASCASPEC. The data was then grouped using GPPHA to get minimum 50 counts per bin so as to use  $\chi^2$  statistics in our spectral analysis. We have also excluded the energy range between 1.7-2.5 because of calibration issues.

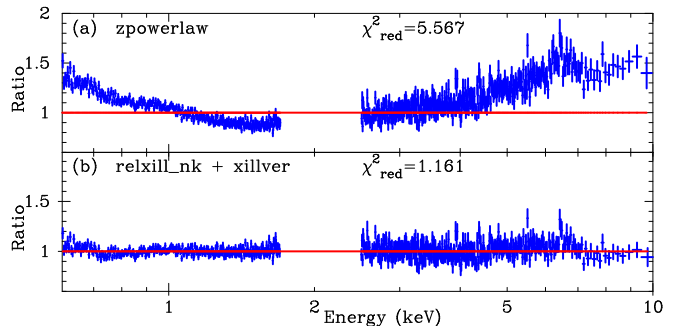


FIG. 7. Data to best-fit model ratios for the spectra models 1 (top panel) and 2 (bottom panel). The reduced  $\chi^2$  is 5.567 and 1.161 in the top and bottom panels respectively. See the text for more details.

### C. Modelling and results

In our analysis, we employed XSPEC v12.10.0c. We fitted the data with the following two models:

MODEL 1: TBABS\*ZPOWERLAW

MODEL 2: TBABS\*(RELXILL\_NK+XILLVER)

Since we are interested here in a qualitative analysis, we report the deviations of  $\delta_1$  only. Studies of deviations of  $\delta_2$  and other deformation parameters will be performed in future.

#### Model 1

Model 1 is: TBABS\*ZPOWERLAW.

TBABS describes the galactic absorption [45] and we fix the galactic column density to  $N_H = 6.74 \cdot 10^{20} \text{cm}^2$ . [46] ZPOWERLAW describes a redshifted photon powerlaw spectrum. The fits were performed in 0.6-10 keV band excluding 1.7-2.5 keV range. We then created the data to best-fit model ratio as shown in panel (a) in Fig. 7 where we can see an excess of photon count at low energies and a broad iron line around 6.4 keV. The best-fit values are reported in the second column in Tab. I, and the data-to-model ratio plots are presented in Fig. 7. The top panel therein unambiguously demonstrate that a strong

Model	1	2
TBABS		
$N_H/10^{20} \text{ cm}^{-2}$	6.74*	6.74*
ZPOWERLAW		
$\Gamma$	$2.858^{+0.003}_{-0.003}$	-
$z$	0.0247*	-
RELXILL_NK		
$q$	-	$> 7.549$
$a_*$	-	$> 0.991$
$i$ [deg]	-	$< 37.50$
$\log \xi$	-	$3.365^{+0.015}_{-0.013}$
$A_{\text{Fe}}$	-	$0.547^{+0.041}_{-0.547}$
$\delta_1$	-	$0.0323^{+0.014}_{-0.011}$
$R$	-	-1
XILLVER		
$\log \xi$	-	0.0*
$\chi^2/dof$	5.567	1.161

TABLE I. Summary of the best-fit values for the spectral models 1 and 2. The reported uncertainty corresponds to the 90% confidence level for one relevant parameter. \* indicates that the parameter is frozen to the value obtained from independent measurements.  $E_{\text{cut}}$  is frozen at 300 keV.

reflected component is present, which is widely attributed to the illumination of the disk by a hot corona. Invoking this paradigm, we proceed to fit the spectrum using our physically motivated spectrum code RELXILL\_NK and XILLVER.

### Model 2

Model 2 is: TBABS\*(RELXILL\_NK+XILLVER).

The reflection spectrum of the disk in the KRZ metric is described by RELXILL\_NK, in which the free parameters were chosen to be the black hole spin  $a_*$ , the deformation parameter  $\delta_1$ , the inclination angle of the disk  $i$ , the emissivity index  $q$  assuming a simple power-law  $1/r^q$  where  $r$  is the radial distance along the disk, the photon index of the primary component from the corona  $\Gamma$ , the ionization of the disk  $\log \xi$ , and the iron abundance  $A_{\text{Fe}}$  (in Solar units). XILLVER describes the reflection spectrum from some cold material at a larger distance from the black hole and is independent of the background metric. [7] We assume the same iron abundance  $A_{\text{Fe}}$  in RELXILL\_NK and in XILLVER. As we can see from panel (b) of Fig. 7, the fit is much better than Model 1. The reduced  $\chi^2$  comes down from 5.567 to 1.161. The best-fit values are reported in third column in Tab. I.

### D. Discussion

We now discuss some aspects of our analysis. In our best-fit model 2, we find a high value of the photon index  $q$ , that is, most of the radiation seems to come from very inner part of the accretion disk. The spin parameter  $a_*$  is always very close to 1. This is consistent with the

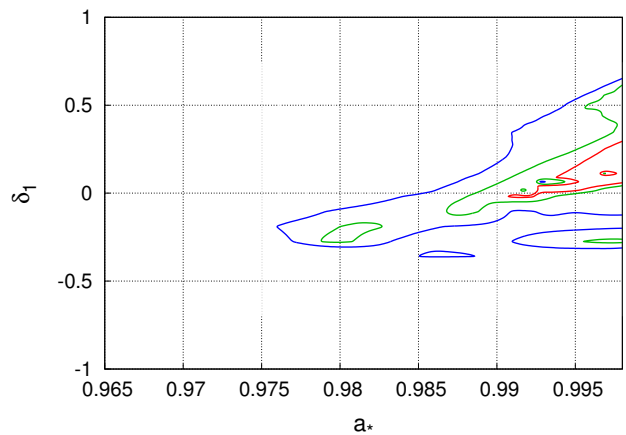


FIG. 8. Constraints on the spin parameter  $a_*$  and the KRZ deformation parameter  $\delta_1$  from the *Suzaku* data of the supermassive black hole in Ark 564 assuming model 2. The red, green, and blue lines indicate, respectively, the 68%, 90%, and 99% confidence level contours for two relevant parameters. See the text for more details.

previous analysis results of Ark 564 and suggests that it is a high spin black hole. The inclination angle of the disk  $i$  is not high. The iron abundance  $A_{\text{Fe}}$  (in units of Solar iron abundance) is less than 1. The non-relativistic component XILLVER describes reflection from a cold gas cloud with  $\log \xi = 0$ . It is subdominant with respect to relativistic component RELXILL\_NK. This permits us to get the measurements of  $a_*$  and of the deformation parameter.

The main goal of our study is to constrain the space-time metric around the supermassive black hole in Ark 564, getting a measurement of  $a_*$  and  $\delta_1$ . Since there exists a degeneracy between  $a_*$  and most non-Kerr parameters, any tests of GR have to contend with the fact that simultaneous measurement of both spin and non-Kerr parameters will have an intrinsic uncertainty. Model 2 very well constrains both the parameters, and the degeneracy is shown in Fig. 8. The red, green, and blue lines indicate, respectively, the 68%, 90%, and 99% confidence level contours for two relevant parameters. The line at  $\delta_1 = 0$  marks the Kerr solution. Since the Kerr solution is included within the smallest uncertainty contours, our results are consistent with the hypothesis that the supermassive object in Ark 564 is a Kerr black hole.

The specific shape of the contours can be understood by realizing that the ISCO contour can be used as a proxy for the degeneracy, especially near the Kerr solution. This is because the reflection spectrum, and thus the degeneracy, is strongly affected by the location of the inner edge of the disk, which in our case is at the ISCO. Far away from the Kerr solution, i.e., for large non-zero values of the deformation parameter, the change in other quantities like redshift is significant, and ISCO by itself ceases to be the dominant quantity in the determination



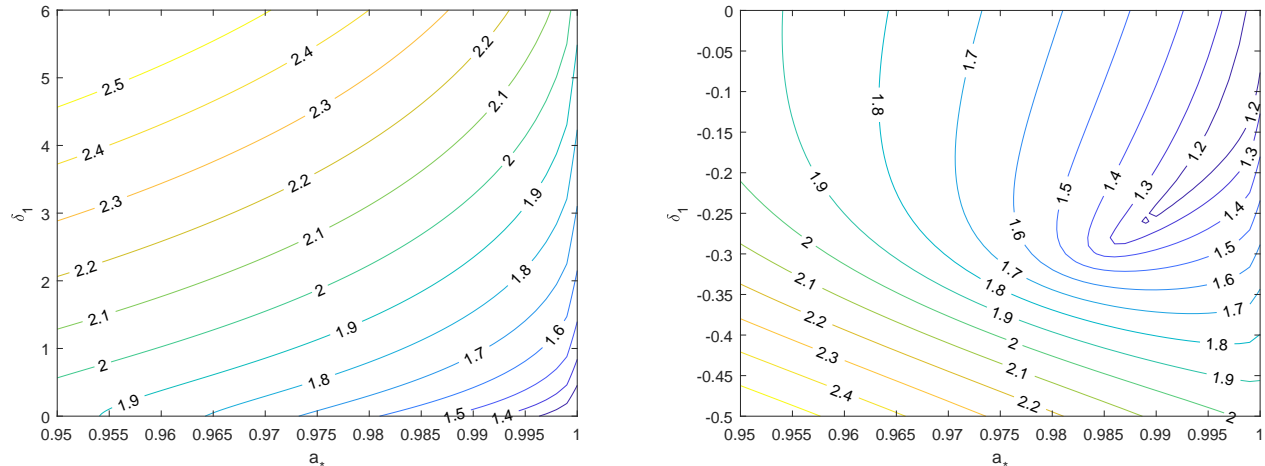


FIG. 9. Impact of  $\delta_1$  on the ISCO radius at high spin, namely  $a_* > 0.95$ . Values of  $r_{\text{ISCO}}$  are indicated on each contour. Upper panel: positive  $\delta_1$ . Bottom panel: negative  $\delta_1$ .

of the degeneracy contours. Fig. 9 shows the contour plot for  $r_{\text{ISCO}}$  with respect to  $\delta_1$  and  $a_*$ , at high spins ( $a_* > 0.95$ ). We can see that the degeneracy contour of Fig. 8 mimics the  $r_{\text{ISCO}} = 1.4M$  ISCO contour.

From Fig. 8, we get the constraints on  $a_*$  and  $\delta_1$ :

$$a_* > 0.975, \quad -0.4 < \delta_1 < 0.7,$$

at 99% confidence interval. For the same dataset, the analysis in [12] had obtained the following constraints on  $\alpha_{13}$  and  $\alpha_{22}$ :

$$a_* > 0.96, \quad -1.0 < \alpha_{13} < 0.2,$$

and

$$a_* > 0.96, \quad -0.1 < \alpha_{22} < 0.9.$$

Another set of constraints on the Johannsen parameter  $\epsilon_3$  is reported in [21]:

$$a_* \geq 0.98, \quad -0.3 < \epsilon_3 < 0.5.$$

We find that the constraints on all the parameters are of the same order of magnitude.

## VI. CONCLUSION

This work presents the introduction of the Konoplya, Rezzolla & Zhidenko metric in the RELXILL\_NK frame-

work. We review the RELXILL\_NK framework and the KRZ metric, followed by a comparison of the new model with existing codes. We study how the transfer function and the iron line spectrum is affected by the KRZ parameters. We apply the new model to a *Suzaku* dataset of the supermassive black hole in the Seyfert I galaxy Ark 564 and obtain constraints on the KRZ parameter  $\delta_1$ . A public version of RELXILL\_NK is available at [47], and we plan to add the KRZ parameters to the public version in near future.

**Acknowledgments** – S.N. acknowledges support from the Excellence Initiative at Eberhard-Karls Universität Tübingen. S.N. and J.A.G. also acknowledge support from the Alexander von Humboldt Foundation. A.B.A. acknowledges the support from the Shanghai Government Scholarship (SGS). A.T. acknowledges support from the China Scholarship Council (CSC), Grant No. 2016GXZR89. This work was supported by the National Natural Science Foundation of China (NSFC), Grant No. U1531117, and Fudan University, Grant No. IDH1512060.

[1] C. M. Will, *Living Rev. Rel.* **17**, 4 (2014), [arXiv:1403.7377 \[gr-qc\]](https://arxiv.org/abs/1403.7377).

[2] C. Bambi, *Rev. Mod. Phys.* **89**, 025001 (2017), [arXiv:1509.03884 \[gr-qc\]](https://arxiv.org/abs/1509.03884).

- [3] LIGO Scientific and Virgo Collaborations, (2019), [arXiv:1903.04467 \[gr-qc\]](#).
- [4] R. P. Kerr, *Phys. Rev. Lett.* **11**, 237 (1963).
- [5] P. T. Chrusciel, J. Lopes Costa, and M. Heusler, *Living Rev. Rel.* **15**, 7 (2012), [arXiv:1205.6112 \[gr-qc\]](#).
- [6] C. Bambi, A. B. Abdikamalov, D. Ayzenberg, Z. Cao, H. Liu, S. Nampalliwar, A. Tripathi, J. Wang-Ji, and Y. Xu, *Universe* **4**, 79 (2018), [arXiv:1806.02141 \[gr-qc\]](#).
- [7] J. García *et al.*, *Astrophys. J.* **782**, 76 (2014), [arXiv:1312.3231 \[astro-ph.HE\]](#).
- [8] T. Dauser *et al.*, *Mon. Not. Roy. Astron. Soc.* **444**, 100 (2014), [arXiv:1408.2347 \[astro-ph.HE\]](#).
- [9] C. Bambi *et al.*, *Astrophys. J.* **842**, 76 (2017), [arXiv:1607.00596 \[gr-qc\]](#).
- [10] A. B. Abdikamalov, D. Ayzenberg, C. Bambi, T. Dauser, J. A. Garcia, and S. Nampalliwar, (2019), [arXiv:1902.09665 \[gr-qc\]](#).
- [11] Z. Cao *et al.*, *Phys. Rev. Lett.* **120**, 051101 (2018), [arXiv:1709.00219 \[gr-qc\]](#).
- [12] A. Tripathi, S. Nampalliwar, A. B. Abdikamalov, D. Ayzenberg, J. Jiang, and C. Bambi, *Phys. Rev.* **D98**, 023018 (2018), [arXiv:1804.10380 \[gr-qc\]](#).
- [13] J. Wang-Ji, A. B. Abdikamalov, D. Ayzenberg, C. Bambi, T. Dauser, J. A. Garcia, S. Nampalliwar, and J. F. Steiner, (2018), [arXiv:1806.00126 \[gr-qc\]](#).
- [14] Y. Xu, S. Nampalliwar, A. B. Abdikamalov, D. Ayzenberg, C. Bambi, T. Dauser, J. A. Garcia, and J. Jiang, *Astrophys. J.* **865**, 134 (2018), [arXiv:1807.10243 \[gr-qc\]](#).
- [15] K. Choudhury, S. Nampalliwar, A. B. Abdikamalov, D. Ayzenberg, C. Bambi, T. Dauser, and J. A. Garcia, (2018), [arXiv:1809.06669 \[gr-qc\]](#).
- [16] M. Zhou, Z. Cao, A. Abdikamalov, D. Ayzenberg, C. Bambi, L. Modesto, and S. Nampalliwar, *Phys. Rev.* **D98**, 024007 (2018), [arXiv:1803.07849 \[gr-qc\]](#).
- [17] M. Zhou, A. Abdikamalov, D. Ayzenberg, C. Bambi, L. Modesto, S. Nampalliwar, and Y. Xu, *EPL* **125**, 30002 (2019).
- [18] A. Tripathi, S. Nampalliwar, A. B. Abdikamalov, D. Ayzenberg, C. Bambi, T. Dauser, J. A. Garcia, and A. Marinucci, (2018), [arXiv:1811.08148 \[gr-qc\]](#).
- [19] A. Tripathi *et al.*, (2019), [arXiv:1901.03064 \[gr-qc\]](#).
- [20] Y. Zhang, A. B. Abdikamalov, D. Ayzenberg, C. Bambi, T. Dauser, J. A. Garcia, and S. Nampalliwar, (2019), [arXiv:1901.06117 \[gr-qc\]](#).
- [21] A. Tripathi, A. B. Abdikamalov, D. Ayzenberg, C. Bambi, and S. Nampalliwar, (2019), [arXiv:1903.04071 \[gr-qc\]](#).
- [22] T. Johannsen, *Phys. Rev.* **D88**, 044002 (2013), [arXiv:1501.02809 \[gr-qc\]](#).
- [23] S. Vigeland, N. Yunes, and L. Stein, *Phys. Rev.* **D83**, 104027 (2011), [arXiv:1102.3706 \[gr-qc\]](#).
- [24] R. Konoplya, L. Rezzolla, and A. Zhidenko, *Phys. Rev.* **D93**, 064015 (2016), [arXiv:1602.02378 \[gr-qc\]](#).
- [25] P. Kanti *et al.*, *Phys. Rev.* **D54**, 5049 (1996), [arXiv:hep-th/9511071 \[hep-th\]](#).
- [26] B. Kleihaus *et al.*, *Phys. Rev.* **D93**, 044047 (2016), [arXiv:1511.05513 \[gr-qc\]](#).
- [27] D. Ayzenberg and N. Yunes, *Phys. Rev.* **D90**, 044066 (2014), [Erratum: *Phys. Rev.* D91, no.6, 069905(2015)], [arXiv:1405.2133 \[gr-qc\]](#).
- [28] A. Maselli *et al.*, *Phys. Rev.* **D92**, 083014 (2015), [arXiv:1507.00680 \[gr-qc\]](#).
- [29] K. D. Kokkotas, R. A. Konoplya, and A. Zhidenko, *Phys. Rev.* **D96**, 064004 (2017), [arXiv:1706.07460 \[gr-qc\]](#).
- [30] S. Nampalliwar, C. Bambi, K. Kokkotas, and R. Konoplya, *Phys. Lett.* **B781**, 626 (2018), [arXiv:1803.10819 \[gr-qc\]](#).
- [31] N. Yunes and F. Pretorius, *Phys. Rev.* **D79**, 084043 (2009), [arXiv:0902.4669 \[gr-qc\]](#).
- [32] K. Yagi, N. Yunes, and T. Tanaka, *Phys. Rev.* **D86**, 044037 (2012), [Erratum: *Phys. Rev.* D89, 049902(2014)], [arXiv:1206.6130 \[gr-qc\]](#).
- [33] R. McNees, L. C. Stein, and N. Yunes, *Class. Quant. Grav.* **33**, 235013 (2016), [arXiv:1512.05453 \[gr-qc\]](#).
- [34] T. Delsate, C. Herdeiro, and E. Radu, *Phys. Lett.* **B787**, 8 (2018), [arXiv:1806.06700 \[gr-qc\]](#).
- [35] A. Sen, *Phys. Rev. Lett.* **69**, 1006 (1992), [arXiv:hep-th/9204046 \[hep-th\]](#).
- [36] K. Hioki and U. Miyamoto, *Phys. Rev.* **D78**, 044007 (2008), [arXiv:0805.3146 \[gr-qc\]](#).
- [37] S. Dastan, R. Saffari, and S. Soroushfar, (2016), [arXiv:1610.09477 \[gr-qc\]](#).
- [38] R. Uniyal, H. Nandan, and K. D. Purohit, *Class. Quant. Grav.* **35**, 025003 (2018), [arXiv:1703.07510 \[gr-qc\]](#).
- [39] Y. Ni, J. Jiang, and C. Bambi, *JCAP* **1609**, 014 (2016), [arXiv:1607.04893 \[gr-qc\]](#).
- [40] C. Bambi, *Black Holes: A Laboratory for Testing Strong Gravity* (Springer, 2017).
- [41] I. D. Novikov and K. S. Thorne, in *Proceedings, Ecole d'Été de Physique Théorique: Les Astres Occlus: Les Houches, France, August, 1972* (1973) pp. 343–550.
- [42] C. T. Cunningham, *Astrophys. J.* **202**, 788 (1975).
- [43] T. Dauser, J. Wilms, C. S. Reynolds, and L. W. Brenneman, *Mon. Not. Roy. Astron. Soc.* **409**, 1534 (2010), [arXiv:1007.4937 \[astro-ph.HE\]](#).
- [44] D. J. Walton, E. Nardini, A. C. Fabian, L. C. Gallo, and R. C. Reis, *Mon. Not. Roy. Astron. Soc.* **428**, 2901 (2013), [arXiv:1210.4593 \[astro-ph.HE\]](#).
- [45] J. Wilms, A. Allen, and R. McCray, *Astrophys. J.* **542**, 914 (2000), [arXiv:astro-ph/0008425 \[astro-ph\]](#).
- [46] “CALCULATE GALACTIC  $N_H$ ,” <http://www.swift.ac.uk/analysis/nhtot/>.
- [47] “RELXILL\_NK,” [http://www.tat.physik.uni-tuebingen.de/~nampalliwar/relxill\\_nk/](http://www.tat.physik.uni-tuebingen.de/~nampalliwar/relxill_nk/).